Available online at www.sciencedirect.com
ScienceDirect
Trans. Nonferrous Met. Soc. China 34(2024) 1571−1587
Transactions of Nonferrous Metals Society of China
www.tnmsc.cn

Influence of Fe content on microstructure and performance of powder metallurgy Cu−Fe alloys

Ping ZHANG[1], Xiao-bo YUAN[1], Zi-ming ZENG[1],
Jian-wei TENG[1], Yun-he ZHOU[2], Biao-biao YANG[1,3,4], Yun-ping LI[1]

1. State Key Laboratory of Powder Metallurgy, Central South University, Changsha 410083, China;
2. Institute for Materials Research, Tohoku University, Sendai 980-8577, Japan;
3. IMDEA Materials Institute, C/Eric Kandel 2, Getafe, Madrid 28906, Spain;
4. Department of Materials Science, Polytechnic University of Madrid/Universidad Politécnica de Madrid, E.T.S. de Ingenieros de Caminos, Madrid 28040, Spain

Received 18 November 2022; accepted 19 July 2023

Abstract: The influence of various Fe contents (5, 10, 20, and 40 wt.%) on the microstructure and properties of powder metallurgy Cu−Fe alloy by spark plasma sintering, subjected to cold rolling and aging treatments, was explored. The results showed that, with increasing Fe content from 5 wt.% to 40 wt.%, the distribution of Fe phase evolved from the discrete spheroid to the continuous stagger, accompanying with its size increasing from 0.29 to 1.20 μm. Accordingly, the yield strength of the aged alloy increased from 411.5 to 788.8 MPa, whilst the electrical conductivity decreased from 62.5% (IACS) to 42.0% (IACS). Moreover, a rule of mixture was proposed to calculate the contribution of Cu matrix, primary Fe phase and secondary Fe phase to the yield strength of the alloy, which works well in the prediction of mechanical properties for Cu−Fe alloys with Fe content higher than10 wt.%.

Key words: Cu−Fe alloy; powder metallurgy; rapid solidification; mechanical properties; strength calculation

1 Introduction

Cu−Fe alloys have been widely used as electromagnetic interference shielding materials and integrated circuit lead frames, owing to their high strength, high conductivity, good electromagnetic performance, and low cost [1,2]. The solid solubility of Fe in Cu matrix is only 3.95 wt.% at 1083 °C [3]. For this, Cu−Fe alloys are generally divided into two parts: low Fe content Cu−Fe alloys (≤4 wt.%) and high Fe content Cu−Fe alloys (≥4 wt.%), which display different performance. To be specific, low Fe content Cu−Fe alloys exhibit relatively low strengths but high conductivities, for which they are widely used as lead frame materials [2,4]. Typical example was reported by LU et al [5], who prepared a C19400 alloy (Cu−2.5Fe−0.1P−0.12Zn, wt.%) possessing a tensile strength higher than 500 MPa and electrical conductivity higher than 70% (IACS). However, high Fe content Cu−Fe alloys exhibit relatively high strengths but low conductivities. Besides, when the Fe content is higher than 20 wt.%, Cu−Fe alloy also displays outstanding magnetic and electromagnetic shielding properties, low thermal expansion coefficients, and superior wear resistance [6,7]. WANG et al [8] prepared Cu10Fe (wt.%) alloy, of which the tensile strength and the electrical conductivity were 608 MPa and 58% (IACS), respectively. For the same alloy, its

Corresponding author: Biao-biao YANG, Tel: +34-662427349, E-mail: biaobiao.yang@imdea.org;
Yun-ping LI, Tel: +86-13807499012, E-mail: lyping@csu.edu.cn
DOI: 10.1016/S1003-6326(24)66492-7

electromagnetic interference shielding effectiveness was found to be stable in the frequency range of 14 kHz−3 GHz at 103.9 dB, as studied by PANG et al [9]. Study by LIU et al [10] on Cu20Fe0.3B (wt.%) alloy revealed that the saturated magnetization is 41.74 A·m^2/kg. ZHANG et al [11] reported that the tensile strength and electrical conductivity of the Cu30Fe alloy after cold rolling were 826 MPa and 38.4% (IACS), respectively. Cu−Fe alloys with high Fe contents are excellent candidates for industrial applications, but serious compositional segregation in solidification limits their applications [2,11,12].

LUO et al [12] reported that Cu−Fe alloys would form two liquid regions, including Cu-rich zone (L1) and Fe-rich zone (L2), during the solidification from the equilibrium phase diagram of Cu−Fe binary alloy, which is a typical metastable immiscible alloy. In the study of MULLIS et al [13], liquid phase separation of Cu−Fe binary system takes place at only 20 °C below the equilibrium liquidus. Therefore, macro-inhomogeneity in composition and/or microstructure is commonly found in Cu−Fe alloys with high Fe contents (≥5 wt.%) [8]. In comparison with the conventional casting, some researchers have reported that Cu−Fe alloys with high Fe contents prepared by powder metallurgy (PM) exhibit a uniform and fine Fe phase [14,15]. Pre-alloyed powders of Cu−Fe alloys were prepared by gas atomization and the powders were sintered into bulk Cu−Fe alloys. The limited size of the pre-alloyed powders and the lower sintering temperature (650−750 °C, note that the equilibrium liquidus is 1084−1538 °C [12]) can significantly limit the macro-segregation behavior caused by the liquid phase separation of Cu and Fe [4,14].

To the best of the authors' knowledge, previous studies on Cu−Fe alloys mainly focused on the inhibition of Fe phase segregation in conventional casting, and the microstructure and properties of a specific Cu−Fe component. There is a lack of systematic research on the effect of Fe content on the microstructure and properties of Cu−Fe alloys by PM. In this work, Cu−*x*Fe (*x*=5, 10, 20 and 40 wt.%) alloys were prepared by PM. The microstructure, electrical conductivity as well as mechanical performance of alloys during the thermomechanical processing were investigated in detail. Besides, a strength calculation method for immiscible Cu−Fe alloys with high Fe contents (>10 wt.%) was proposed and validated.

2 Experimental

High purity electrolytic Cu (99.99% or 4N) and high purity Fe (99.9% or 3N) were used to fabricate Cu−Fe alloy powders by gas atomization (argon). The nominal compositions of pre-alloyed powders were Cu5Fe, Cu10Fe, Cu20Fe and Cu40Fe (wt.%). Powders of the four alloys were sintered by vacuum spark plasma sintering (SPS, LABOX−325R, Japan). During the sintering process, the pressure first increased to 10 MPa and the temperature accordingly raised to 600 °C under a speed of 100 °C/min. Then, the pressure increased from 10 to 40 MPa accompanying with the temperature rising from 600 to 750 °C. The sintering was conducted at 750 °C for 10 min. It has previously been reported that the high vacuum in the sintering process and the use of graphite mold can protect the powder from oxidation as well as decompose the oxides produced on the surface of the powder [16]. The size of as-sintered sample was *d*30 mm × 10 mm. It was subsequently cold-rolled (CR) with a reduction of 80% and then aged (AG) at 450 °C for 0−16 h.

The compositions of four alloy powders were tested by inductively coupled plasma spectrometer (ICP, SPECTRO BLUE, Germany), as tabulated in Table 1. The mechanical properties and electrical conductivity of alloys after rolling properties and heat treatments were tested at room temperature. The electrical conductivity of the samples was measured by the double-bridge method (QJ84A Zhengyang, China). Each sample was measured three times, and the average value was taken as the recorded electrical conductivity of the tested sample. The hardness of the sample was measured with an HV−5 Vickers hardness tester (200HV−5 Huayin, China). The load of the hardness tester was 1 kg, and the loading time was 10 s. The hardness values of 7 points were randomly measured from different regions in each sample, and the average value was taken as the recorded hardness value of that tested sample. The mechanical properties of alloys were performed on a material testing machine (UTM 5105, China). Tensile tests were conducted at room temperature with a strain rate of 1×10^{-3} s^{-1}.

Table 1 Actual compositions of four alloy powders by ICP

Alloy	Content/wt.%		
	Fe	O	Cu
Cu5Fe	4.8	0.0201	Bal.
Cu10Fe	9.63	0.0532	Bal.
Cu20Fe	18.7	0.0387	Bal.
Cu40Fe	36.8	0.0302	Bal.

Microstructures were characterized by a scanning electron microscope (SEM, FEI Quanta 650, USA) equipped with an energy dispersive X-ray spectrometer (SEM−EDX) and Oxford Instruments Aztec HKL detector. Data acquisition software (HKL Channel 5, Denmark) was used to analyze electron backscattered diffraction (EBSD) raw data. The field emission transmission electron microscope (TEM, Talos F200S, USA) with an operating voltage of 200 kV was utilized to further characterize the nanoscale precipitates. The dislocation density of the sample was calculated by X-ray diffractometer (XRD, D/max 2550 VB, Japan) with a scanning speed of 8 (°)/min.

3 Results

3.1 Microstructures

Both the morphology and cross-sectional microstructure of Cu−*x*Fe (*x*=5, 10, 20 and 40 wt.%) powders were characterized and shown in Fig. 1. All alloy powders were spherical, and the fine dispersed Fe phase can be seen in the matrix on the cross-section of the powder. The average particle size was 66.9, 52.3, 53.4, and 59.5 μm, respectively, as the Fe content increases from 5 to 10, 20, and 40 wt.%, respectively. Besides, as a protective argon atmosphere was used in the process of the atomization, the oxygen content of the powders (as shown in Table 1) was less than 0.05 wt.% and should weakly affect the subsequent mechanical performance.

Backscattered electron images (BEI), and the corresponding elemental distribution maps of SPS-ed Cu−Fe alloys are shown in Fig. 2. During the solidification of Cu−Fe alloys, liquid phase separation occurred first, giving rise to the formation of primary Fe phase and Cu phase matrix [12,13]. With the decrease of temperature, the secondary Fe phase in nanometer size will precipitate in the Cu matrix [3,8]. Fe particles shown in Figs. 2(a−d) were primary Fe phase. Besides, all alloys exhibited similar microstructures, and the Fe particles (the primary Fe) were all embedded in the Cu matrix randomly. However, with the increase of Fe content, the size and number fraction of Fe particles increased distinctly. Meanwhile, the shape of the primary Fe particles was sensitive to the Fe content. To be specific, for Cu5Fe and Cu10Fe alloys, the primary Fe phase was basically spherical and uniformly dispersed, whilst the discontinuously ellipsoidal primary Fe phase was found in Cu20Fe and Cu40Fe alloys.

Microstructures of SPS-ed Cu−Fe alloys after cold rolling were presented in Fig. 3. After cold rolling, Fe particles were stretched along the rolling

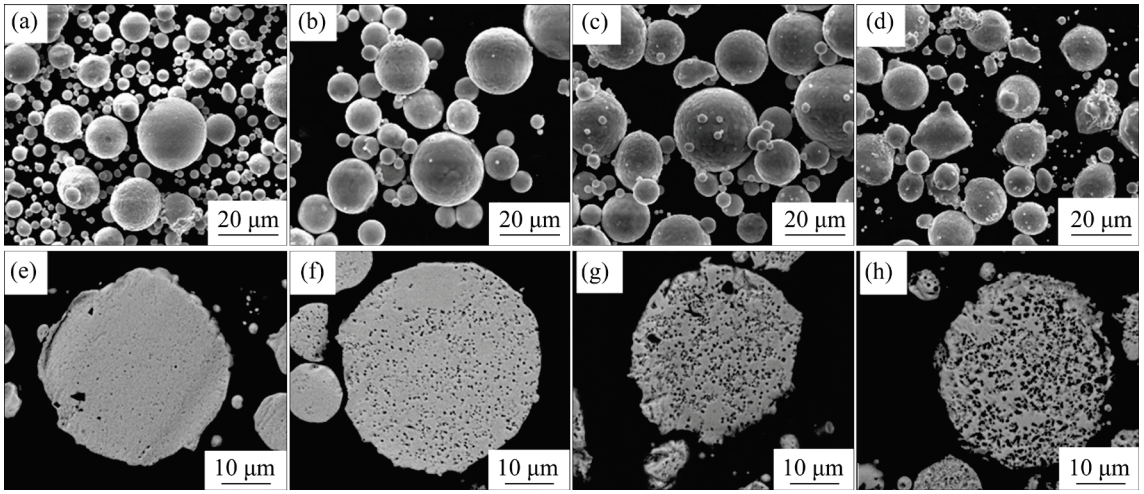

Fig. 1 Morphology (a−d) and cross-section microstructure (e−h) of Cu−Fe alloy powders with different Fe contents: (a, e) Cu5Fe; (b, f) Cu10Fe; (c, g) Cu20Fe; (d, h) Cu40Fe

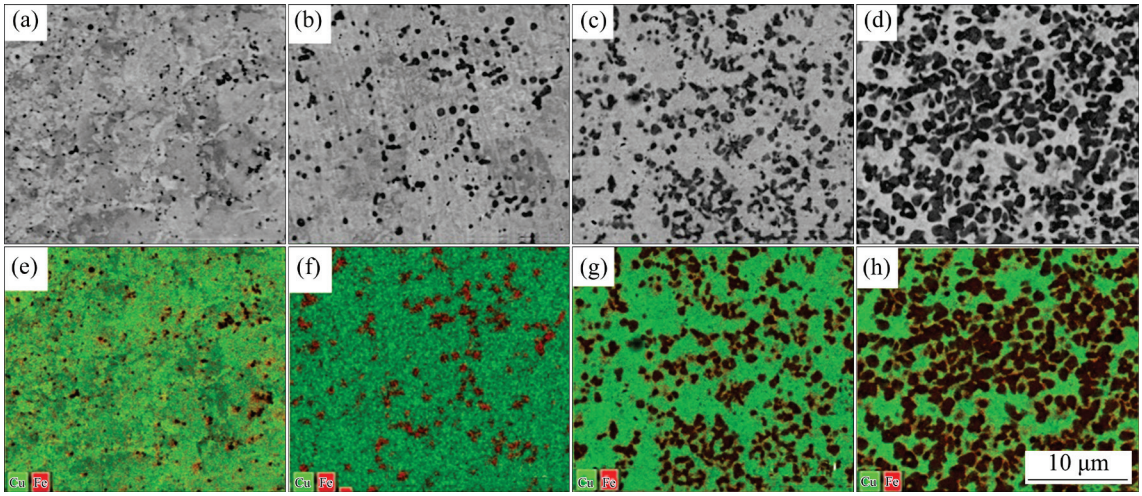

Fig. 2 Backscattered electron images (a−d) and elemental distribution maps (e−h) of SPS-ed Cu−Fe alloys with different Fe contents: (a, e) Cu5Fe; (b, f) Cu10Fe; (c, g) Cu20Fe; (d, h) Cu40Fe

Fig. 3 Backscattered electron images (BEI) of SPS-ed Cu−Fe alloys after cold rolling: (a) Cu5Fe; (b) Cu10Fe; (c) Cu20Fe; (d) Cu40Fe

direction for all alloys, while this phenomenon seems to be more obvious for the alloy with a high Fe content. For example, for the Cu40Fe alloy, irregular Fe particles were severely broken and elongated along the rolling direction. Moreover, Cu and Fe phases were simultaneously elongated and staggered, forming long and continuous fibers. This difference in variation of microstructure after rolling can be ascribed to different Fe contents.

Figure 4 shows XRD patterns of various Cu−Fe alloys after cold rolling and subsequent aging at 450 °C for 6 h. Apparently, both face-centered cubic (FCC) Cu phases and body-centered cubic (BCC) Fe phases were examined for all Cu−Fe alloys. However, the intensity of peak corresponding to Fe phase increased gradually with the increase of Fe content, which was in line with the results in Fig. 3.

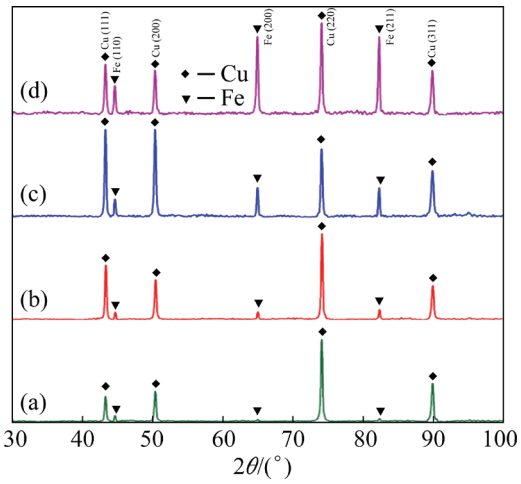

Fig. 4 XRD patterns of various Cu−Fe alloys after cold rolling and aging at 450 °C for 6 h: (a) Cu5Fe; (b) Cu10Fe; (c) Cu20Fe; (d) Cu40Fe

Given the analysis of X-ray diffraction is semi-quantitative as well as generally limited by the spatial resolution, further high-resolution TEM characterization was performed on various Cu−Fe alloys (subjected to cold rolling and aging at 450 °C for 6 h), with the results shown in Figs. 5 and 6. Obviously, for Cu5Fe and Cu10Fe alloys, the major Fe phase was observed in the form of spherical particles, and no Fe grains were detected. However, unlike the Cu−Fe alloy with a low Fe content, clear and large Fe grains were detected for Cu20Fe and Cu40Fe alloys. Besides, the spherical primary Fe phase particles were observed in both alloys. Only one ellipsoidal Cu particle was observed in Cu40Fe alloy in Fig. 6.

TEM characterization with a higher magnification, to explore if the nanoscale precipitate exists or not, was also performed for various Cu−Fe alloys (Fig. 7). Obviously, the spherical particles in various sizes could be observed in all Cu−Fe alloys. NIU et al [17] reported that the layered structure of Cu and Fe experienced drastic thermal grooving and rapid grain growth when temperature was higher than 500 °C. For this, it is highly possible that during aging at 450 °C, the deformed Fe phase will not curl and spheroidize. Therefore, the spherical particles with a relatively large size (50−200 nm) should be the primary Fe phase, which was formed during the solidification. Besides, the particles with a size below 10 nm should be the secondary Fe phase, which appeared during the aging treatment. The nano-sized Fe phase was found in all Cu−Fe alloys. Fe phase was formed by the precipitation of Fe atoms from the Cu-rich matrix [3,12]. At a given temperature, the residual Fe content in the Cu

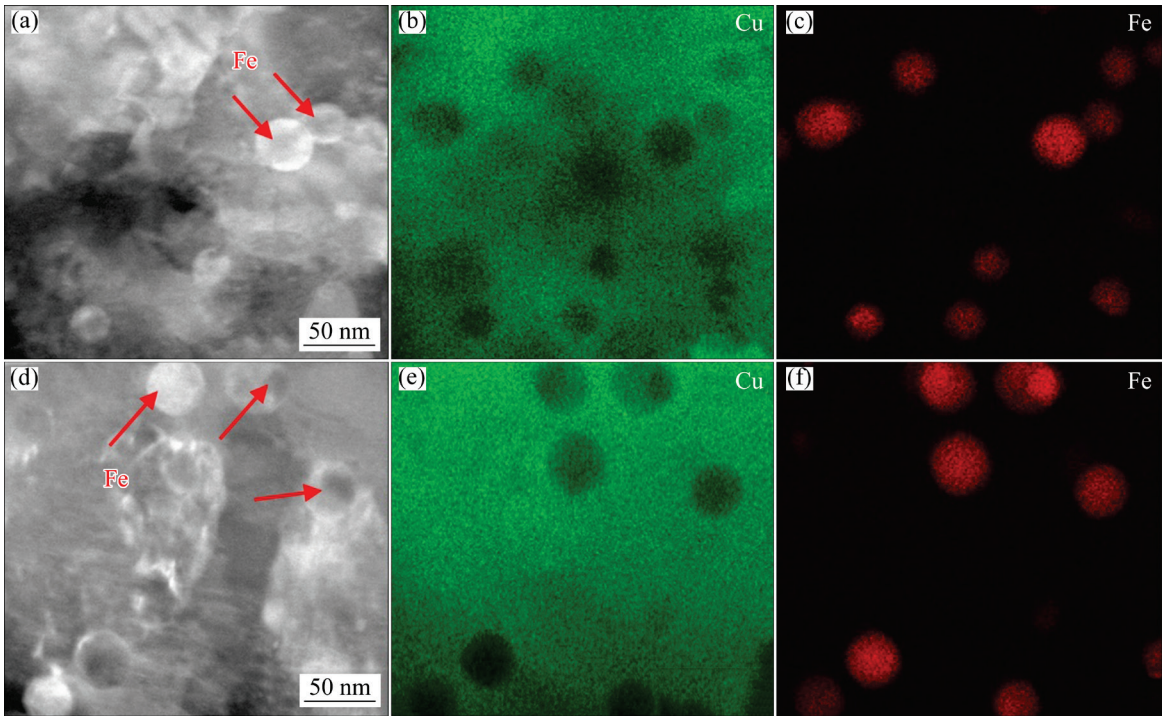

Fig. 5 TEM images of Cu−Fe alloys after cold rolling and aging (a, d), and corresponding EDS mappings of Cu (b, e) and primary Fe (c, f) phases: (a−c) Cu5Fe alloy; (d−f) Cu10Fe alloy

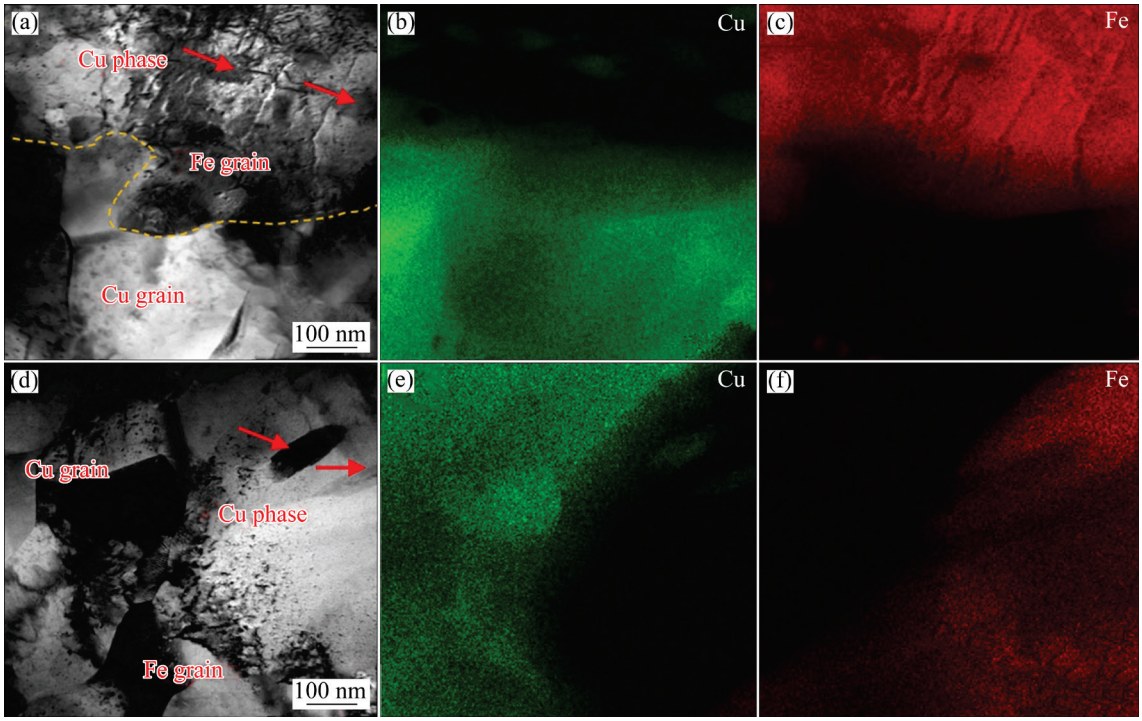

Fig. 6 TEM images of Cu−Fe alloys after cold rolling and aging (a, d), and corresponding EDS mappings of Cu (b, e) and Fe (c, f) grains: (a−c) Cu20Fe alloy; (d−f) Cu40Fe alloy

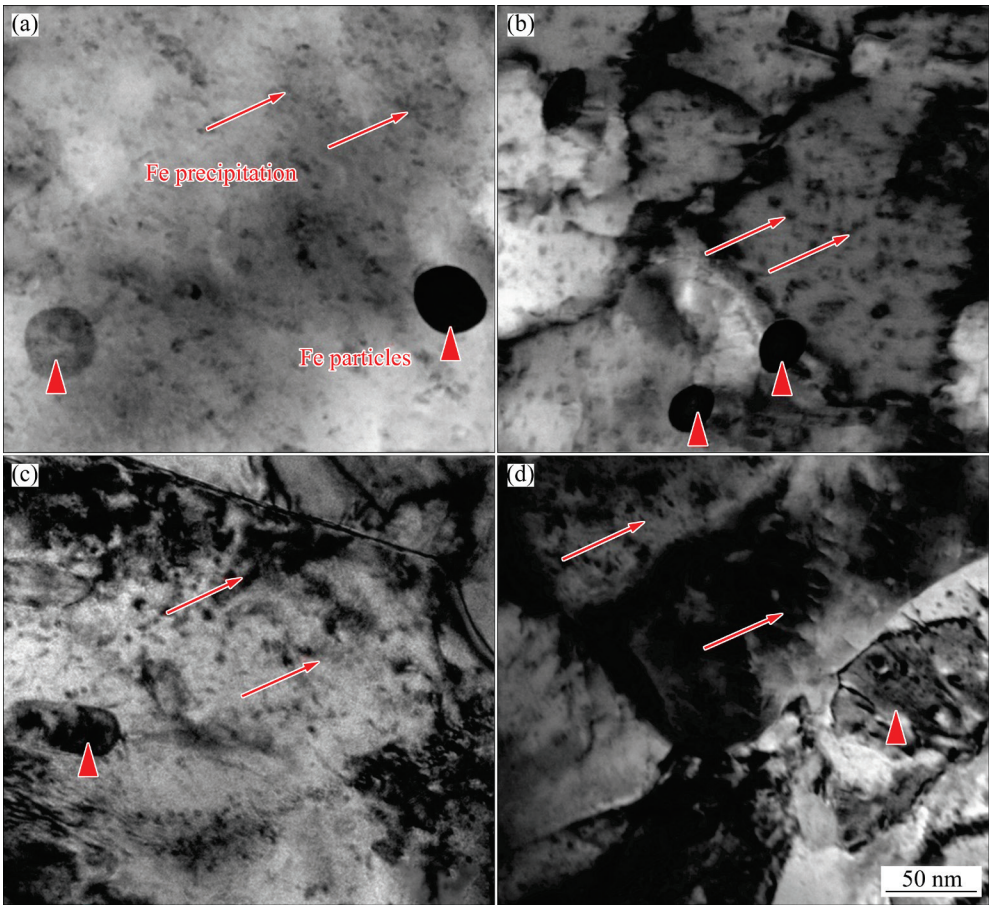

Fig. 7 TEM images of Cu−Fe alloys after cold rolling and aging at 450 °C for 6 h: (a) Cu5Fe; (b) Cu10Fe; (c) Cu20Fe; (d) Cu40Fe (Arrows represent Fe precipitates and triangles represent Fe particles)

matrix was reported to increase with increasing the Fe content in Cu−Fe alloy [18]. In addition, from the perspective of precipitation kinetics, the precipitation behavior of Cu−Fe alloy with a high Fe content should be easier than that of Cu−Fe alloy with a low Fe content [19,20]. Therefore, with the increase of Fe content, the fraction of Fe phase increased.

The orientation relationship (OR) between nano-sized Fe phase and Cu matrix was analyzed by high-resolution transmission electron microscopy (HRTEM) and fast Fourier transform (FFT). In this work, Cu5Fe alloy was taken as an example for this specific analysis. For one thing, the Fe phase with a size of ~20 nm in Fig. 8(a) was incoherent with Cu matrix, and the crystal orientation relationship between them can be given as $[\bar{1}23]BCC_{Fe}$// $[011]FCC_{Cu}$. For the other thing, the Fe phase with a smaller size of ~7 nm in Fig. 8(d) exhibited the FCC crystal structure and was completely coherent with Cu matrix. The OR can be determined as $[011]_{Fe}$//$[011]_{Cu}$ and $(111)_{Fe}$//$(111)_{Cu}$. Both the coherent and noncoherent ORs between Fe phases and Cu matrix were also observed in the other Cu−Fe alloys, consistent with previous studies [4,9,15]. Besides, nanotwins were also observed in Fig. 8(d), which was believed to increase the mechanical properties but not decrease the electrical conductivity of Cu alloy [21]. Similar to the ORs, there was no obvious correlation between the appearance of nanotwins and the Fe content in Cu−Fe alloy.

3.2 Mechanical and electrical properties

Figure 9 shows the true stress−true strain curves as well as the evolution of yield strength (YS) and elongation with respect to the Fe content for the SPS-ed Cu−Fe alloys. The yield strength increased gradually with increasing Fe content, with the values of 206, 266, 335, and 512 MPa, for Cu5Fe, Cu10Fe, Cu20Fe, and Cu40Fe, respectively.

To further improve the comprehensive properties of the alloy, cold rolling and heat treatment were applied to the SPS-ed Cu−Fe alloys. The evolutions of hardness and conductivity of the alloy aged at 450 °C are shown in Fig. 10, with respect to the aging time. As the aging time increases, the hardness decreased slightly, but the conductivity increased obviously. After aging for 6 h, the conductivity of Cu5Fe and Cu40Fe alloys increased from 39.99% (IACS) to 62.47% (IACS) and from 24.53% (IACS) to 41.49% (IACS), respectively.

Figure 11 shows the true stress−true strain curves as well as the evolution of YS and elongation with respect to the Fe content for the Cu−Fe alloys

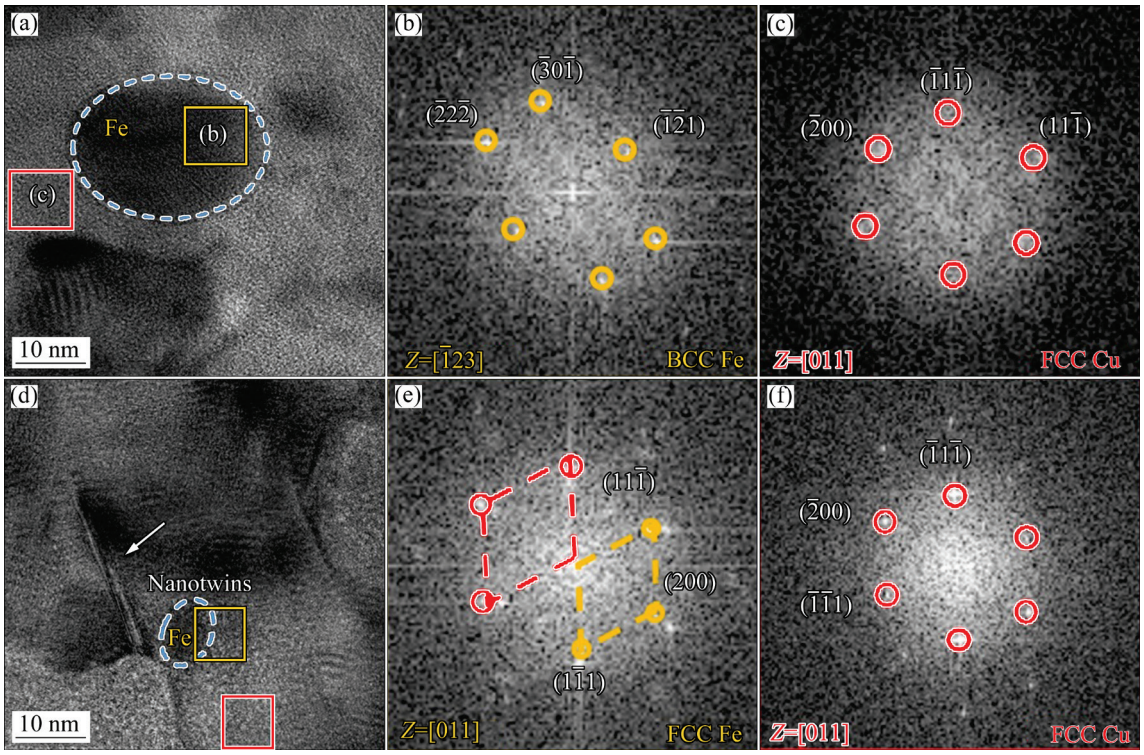

Fig. 8 HRTEM images (a, d) and corresponding FFT patterns (b, c, e, f) of Cu5Fe alloy

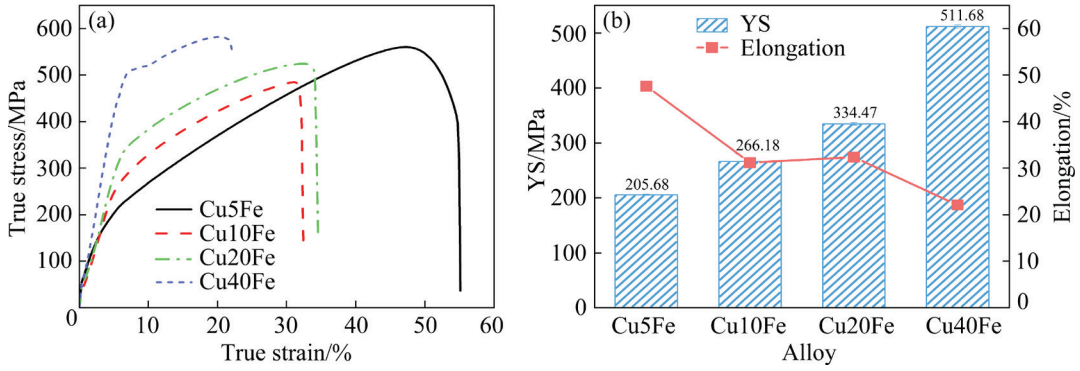

Fig. 9 True stress−true strain curves of SPS-ed Cu−Fe alloys (a) and evolution of yield strength (YS) and elongation with respect to Fe content (b)

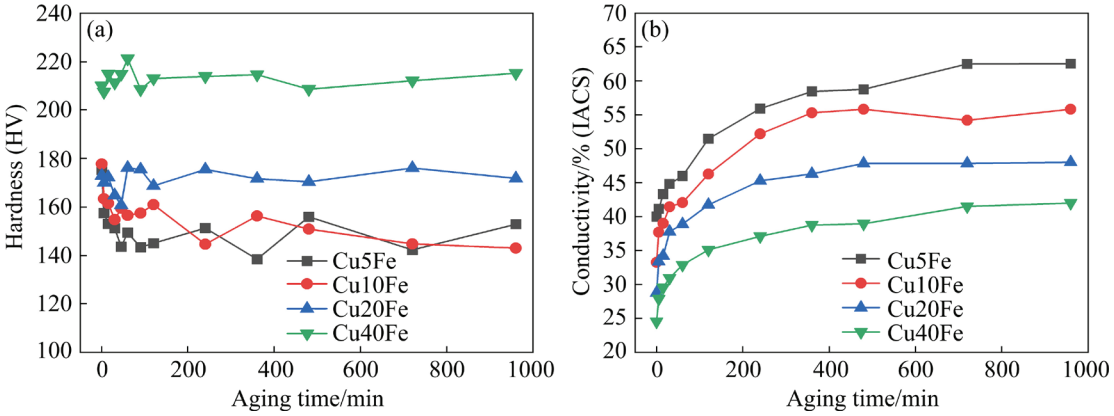

Fig. 10 Variation of hardness (a) and conductivity (b) of cold-rolled Cu−Fe alloys aged at 450 °C for various time

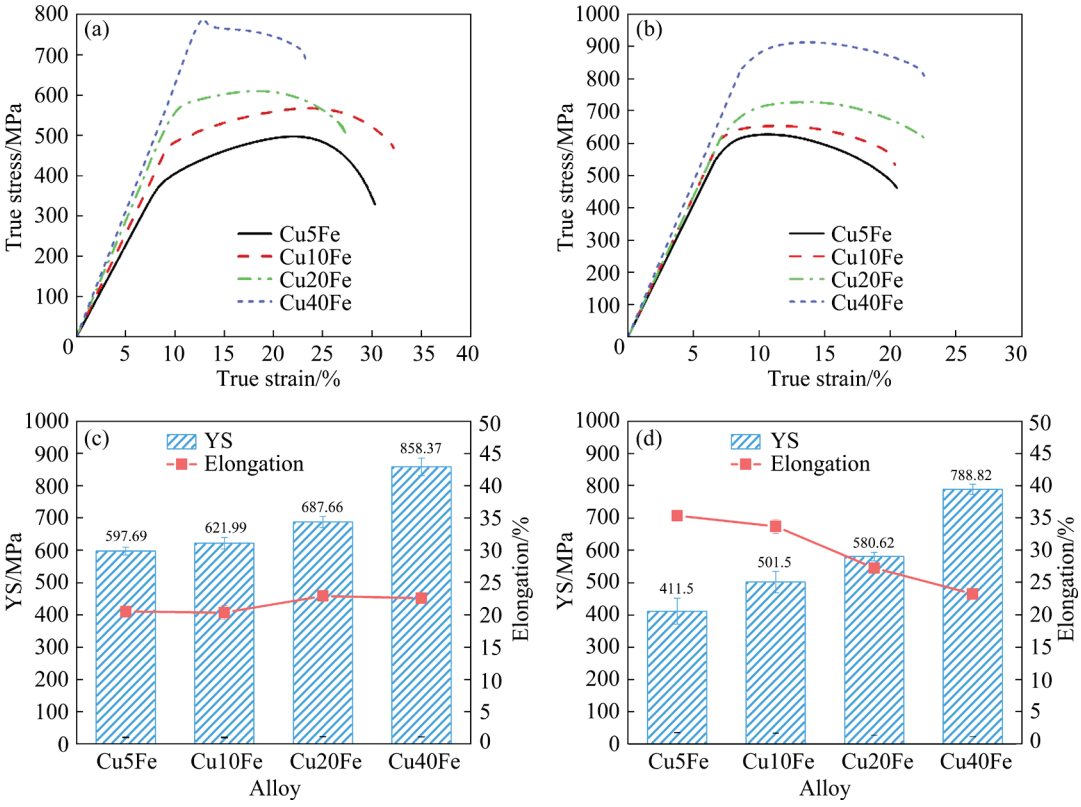

Fig. 11 True stress−true strain curves of Cu−Fe alloys after CR (a) and CR+AG at 450 °C for 6 h (b); variation of YS and elongation of Cu−Fe alloys after CR (c) and CR+AG at 450 °C for 6 h (d)

after CR (cold rolling) and CR+AG (aging). As Fe content increased, the YS of Cu−Fe alloy after CR or CR+AG increased distinctly. Meanwhile, the elongation of Cu−Fe alloy after CR changed slightly, whilst an obvious decline was found for the Cu−Fe alloy after CR+AG. Under the same Fe content, the aging treatment can decrease the YS, but improve the elongation via decreasing the dislocation densities [8,22]. The highest elongation was found for Cu5Fe after CR+AG, but the highest strength was found for Cu40Fe alloy after CR.

4 Discussion

4.1 Effect of Fe content on microstructures of Cu−Fe alloys

For the SPS-ed alloys, Fe content plays a significant role in the morphology of the primary Fe phase and the grain size of the Cu matrix. Feret diameters of the primary Fe phase in SPS-ed alloys were statistically plotted in Fig. 12. The mean diameters of Fe particles in Cu5Fe, Cu10Fe, Cu20Fe, and Cu40Fe alloys are 0.29, 0.41, 0.80, and 1.20 μm, respectively. As the Fe content increases, the size of Fe particles increases. Figures 13(a−d) show Fe phase and grain boundaries (GBs) maps of various SPS-ed Cu−Fe alloys. With the increase of Fe content from 5 to 40 wt.%, no significant change regarding the grain size of Cu matrix is found (1.45−1.99 μm); however, the grain size of Cu matrix for Cu40Fe (0.73 μm) is significantly lower that for the other Cu−Fe alloys,

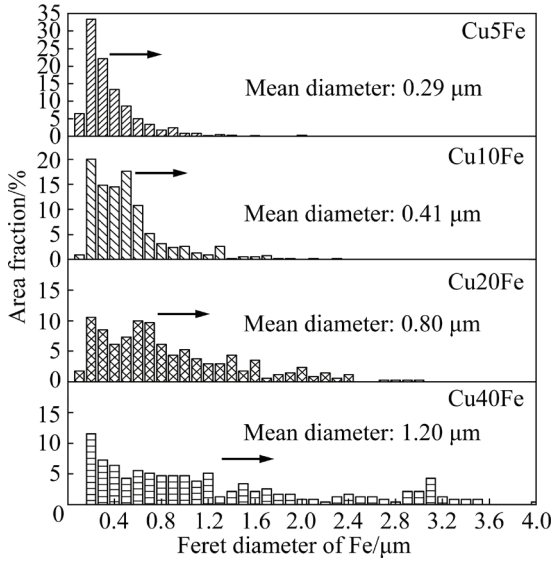

Fig. 12 Feret diameter of primary Fe phase in SPS-ed alloys with different Fe contents

as shown in Figs. 13(e−h).

The Cu−Fe binary system has a large metastable miscibility gap. SHI et al [23] reported that during the liquid phase separation of Cu−Fe binary alloy, when the volume fraction of the two phases is close to each other (Cu40Fe in this work), the interpenetrating or bicontinuous structure will be formed. Interlaced phase interfaces hinder the expansion of the two-phase grain boundaries, thus inhibiting the growth of grains during solidification. Nevertheless, when the volume fractions of the two phases differ greatly (Cu5Fe, Cu10Fe, and Cu20Fe in this work), a few phases in the liquid phase separation stage will form discrete cores firstly, and then grow gradually during the solidification process. Therefore, the grain size of Cu40Fe alloy is smaller.

The reduction of the grain size increases dislocation accumulation and decreases dislocation mean free path in Cu40Fe [24]. The primary Fe phase is distributed along the GBs of Cu matrix in Cu5Fe, Cu10Fe, and Cu20Fe alloys. There are a lot of disconnections and vacancies at the grain boundary, which provide sites for the nucleation of Fe phase [4,25]. In Cu40Fe, the Fe phase is uniformly doped in the Cu matrix, covering most of the Cu GBs.

Furthermore, the microstructure of Cu−Fe alloy after cold rolling also depends on the Fe content. After 80% rolling deformation, the refinement of Fe particles in Cu−Fe alloys is more obvious with increasing Fe content. We take Cu5Fe and Cu40Fe alloys as examples to demonstrate this viewpoint. In Cu40Fe, both Fe and Cu phases are stretched along the deformation direction to be strip or ribbon in Fig. 3(d). However, the Fe phase in Cu5Fe alloy is still ellipsoidal and slightly elongated in the rolling direction, as shown in Fig. 3(a).

Compared with Cu phase, Fe phase is hard and difficult to deform. During the cold rolling process, Cu matrix preferentially accommodates the plastic deformation. Fe particles will undergo both plastic deformation and shear fracture [26]. Figure 14 demonstrates schematic diagrams of Fe particles (primary Fe phase) refinement mechanism in both Cu5Fe and Cu40Fe alloys. In Cu5Fe alloy, the Fe phase is regular spherical and evenly distributed at the GB and in the crystal (Fig. 14(a)). During the rolling, the Fe phase is subjected to the compressive

stress of the Cu phase and plastic deformation occurs [27]. Both Cu grain and Fe phases are elongated in the rolling direction. In Cu40Fe alloy, the primary Fe phase not only has small spherical particles, but also exists in the form of coarse Fe grains (Fig. 14(c)). The large Fe phase is composed of several Fe grains, which will be refined into several dispersed Fe grains during deformation. The

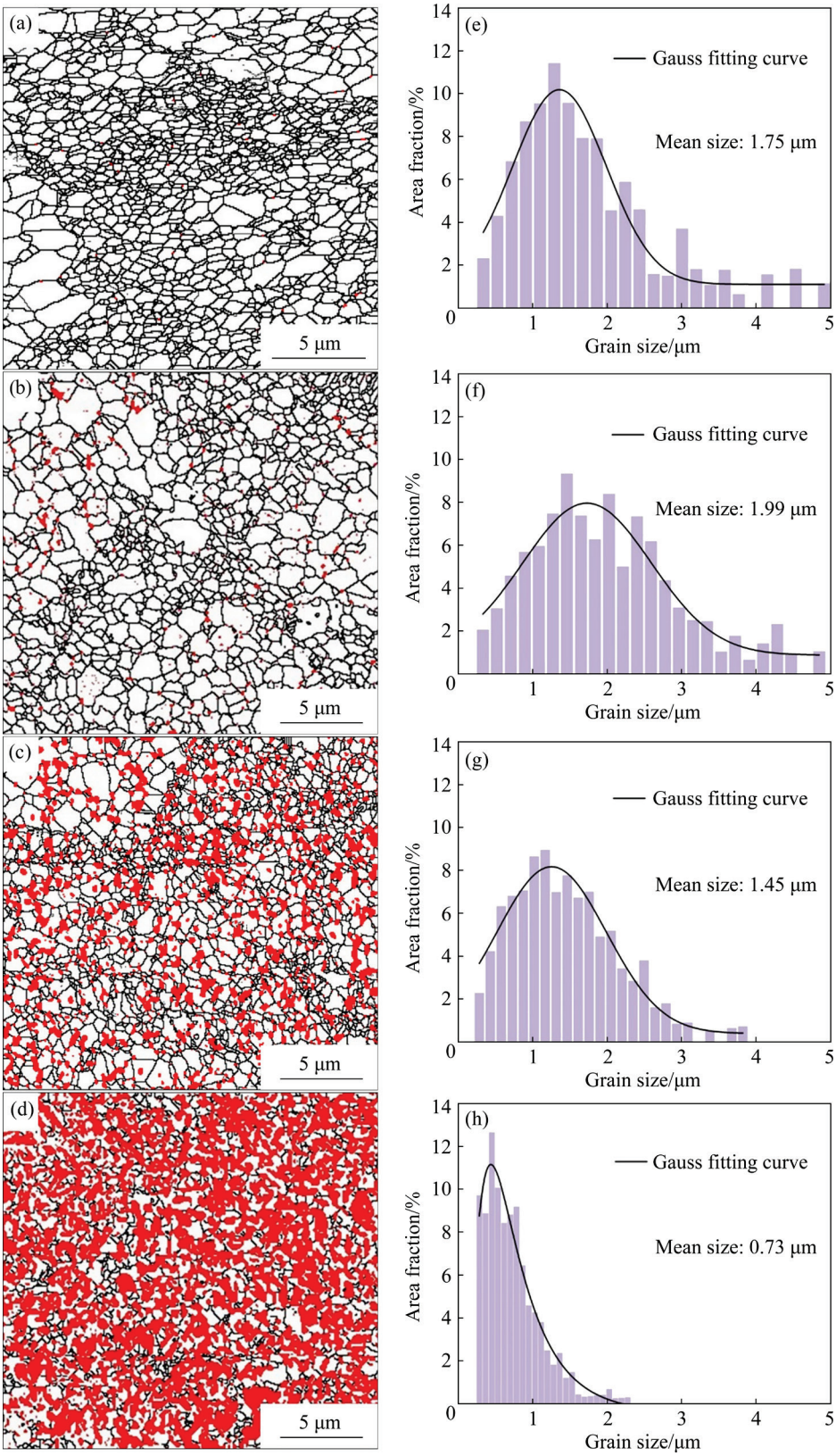

Fig. 13 Fe phase and GBs maps of SPS-ed Cu−Fe alloys (a−d) and variation of Cu grain size distribution (e−h): (a, e) Cu5Fe; (b, f) Cu10Fe; (c, g) Cu20Fe; (d, h) Cu40Fe

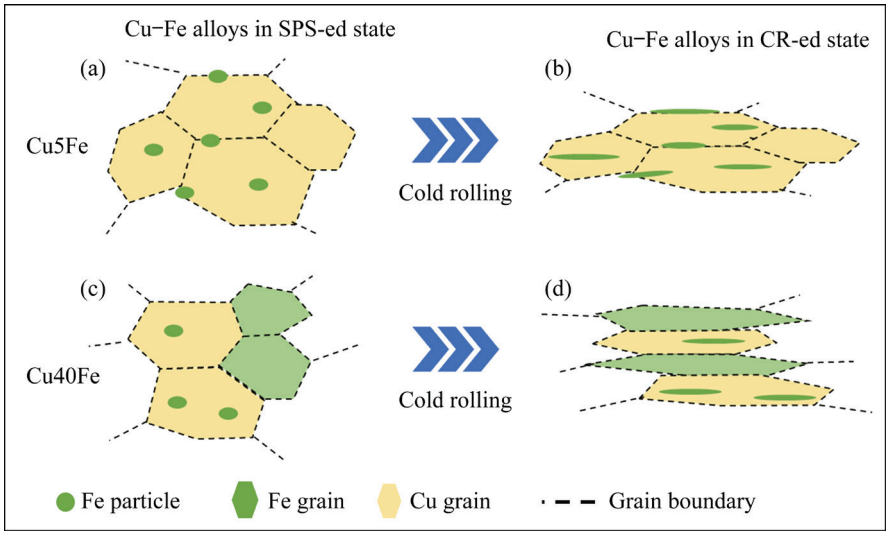

Fig. 14 Schematic diagrams showing refinement mechanism of Fe particles (primary Fe phase) in Cu5Fe (a, b) and Cu40Fe (c, d) alloys at SPS-ed state (a, c) and after CR (b, d)

dispersed Fe and Cu grains are elongated in the rolling direction to form parallel fibers (Fig. 14(d)). This is because the primary Fe phase in Cu5Fe alloy is spherical particles, which have a good pressure-bearing capacity during deformation and are hard to deform [22]. However, the primary Fe phase in Cu40Fe alloy is mainly irregular long rod-shaped particles, which are composed of one or several Fe grains. During the deformation, these particles will fracture along the GB [27], and Fe phase is refined and dispersed. Therefore, under the same deformation degree, the refinement degree and deformation degree of Fe phase in Cu−Fe alloy with a higher Fe content are higher.

4.2 Effect of Fe content on mechanical properties of Cu−Fe alloys

In this work, the mechanical properties of the Cu−Fe alloys are closely related to the Fe content. To further explore their relationship, the strengthening mechanisms of both SPS-ed and cold-rolled Cu−Fe alloys were discussed.

4.2.1 Strengthening mechanisms of SPS-ed Cu−Fe alloys

Cu−Fe alloys with different Fe contents were fabricated by pre-alloyed powder and SPS sintering. After SPS sintering, all Cu−Fe alloys have reached a relatively high density (>99.59%). Under the SPS-ed state, the main strengthening mechanisms of the alloys are solution strengthening and GB strengthening. The yield strength caused by solution strengthening ($\Delta\sigma_{\text{solid solution}}$) can be expressed as [8]

$$\Delta\sigma_{\text{solid solution}}=G\left(|\delta|+\frac{1}{20}\right)|\eta|^{\frac{3}{2}}\sqrt{\frac{x_{\text{a}}}{3}} \tag{1}$$

$$\eta=\frac{\mathrm{d}\ln G}{\mathrm{d}x}=\frac{1}{G}\cdot\frac{\mathrm{d}G}{\mathrm{d}x} \tag{2}$$

where G is the shear modulus of Cu matrix, δ is the factor of lattice change, η is the shear modulus change factor caused by alloying, x_{a} or x is the molar fraction of the solute atoms in the matrix. Solid solution atoms can improve yield strength by causing lattice distortion of the matrix and hindering dislocation movement. In Cu10Fe alloy, WANG et al [8] found that the strengthening of the Cu matrix by the solid solution of Fe is only about 1.2 MPa. In the Cu20Fe alloy, YANG et al [28] reported that the deviation of (111) Cu crystal plane spacing between the measured value and the standard value is ±0.001 Å. These reveal that the Cu matrix lattice is basically undistorted, indicating that the solid solution strengthening effect of Fe atoms in Cu is negligible. Therefore, the total yield strength of the SPS-ed Cu−Fe alloy is simplified as

$$\sigma=\sigma_0+\Delta\sigma_{\text{H–P}} \tag{3}$$

where σ_0 is the intrinsic lattice strength (50 MPa for the Cu alloy) [22], and $\Delta\sigma_{\text{H–P}}$ is the grain boundary strengthening strength and can be calculated as follows:

$$\Delta\sigma_{\text{H–P}}=kd^{-1/2} \tag{4}$$

where k is the Hall−Petch coefficient (k is 0.18 MPa·m$^{1/2}$ for Cu alloys [29]), and d is the mean grain size measured by EBSD images [30,31].

The yield strengths of Cu alloys were calculated by Eqs. (3) and (4), as presented in Fig. 15. The difference between the calculated value (σ_{c1}) and the experimental value (σ_{exp}) increases with the increase of Fe content (Fig. 15(a)). This is because the contribution of Fe to the yield strength of alloy increases with the increase of Fe content, and the contribution of Fe to the strength is not calculated in Eq. (3). Except for Cu5Fe, the error rate between the calculated strength (σ_{c1}) and the experimental strength (σ_{exp}) of other alloys is more than 30%. Obviously, this calculation method is no longer applicable to Cu−Fe alloys with high Fe content. RABADIA et al [32] reported that relatively high strength phase (the Fe phase in this work) and adequate volume fraction can enhance the mechanical properties. Therefore, we should consider the contribution of the existence of Fe phase to the strength.

For the Cu−Fe alloys, Cu and Fe phases are basically immiscible at room temperature, and Cu−Fe alloys are also known as in-situ composites. It is generally accepted that the strength of a composite obeys the rule of mixture (ROM). The strength of SPS-ed Cu−Fe alloy calculated by ROM could be expressed as

$$\sigma_{ROM}=\sigma_{Cu}\varphi_{Cu}+\sigma_{Fe}\varphi_{Fe} \quad (5)$$

where σ_{Cu} and σ_{Fe} are the strengths of Cu and Fe phases, respectively; φ_{Cu} and φ_{Fe} are the corresponding volume fractions. φ_{Cu} and φ_{Fe} are calculated by Eqs. (3) and (4). The k_{Cu} and $\sigma_{0,Cu}$ in σ_{Cu} are the same as that of Cu alloys [22−24]. The k value of 0.6 MPa·m$^{1/2}$ was reported in numerous previous studies on grain refinement strengthening of ferritic steels [25−27]. Therefore, in this work, the k_{Fe} in σ_{Fe} is 0.6 MPa·m$^{1/2}$, and $\sigma_{0,Fe}$ is 100 MPa [33−35]. It can be seen from Fig. 15(a) that the calculated values of ROM (σ_{ROM}) are close to the experimental values of yield strength (σ_{exp}). For high Fe Cu−Fe alloys, the rule of mixture can accurately predict the yield strength of the SPS-ed Cu−Fe alloys. The contribution of Cu and Fe phases to the yield strength of the alloy is shown in Fig. 16. Grain boundary strengthening caused by Fe phase is the main factor for the increase of yield strength, which explains well the phenomenon that the higher the Fe content, the higher the yield strength.

4.2.2 Strengthening mechanisms of Cu−Fe alloys after cold-rolling and aging

The properties of SPS-ed Cu−Fe alloy can be further improved via cold rolling and aging. Similar conclusion was drawn for the Cu−Fe and Cu−Nb alloys [26,27]. Specifically, there is a Hall−Petch relationship between the strength of alloys after deformation and the spacing between the Fe and Nb filaments. The calculation formula of its strength is as follows [27,36]:

$$\Delta\sigma=\sigma_0+k\lambda^{-1/2} \quad (6)$$

where λ is the spacing between filaments. The Hall−Petch coefficient is related to the alloying composition and deformation procedure [27,37]. In this work, due to the low strain processing, the Fe phase in Cu5Fe, Cu10Fe, and Cu20Fe alloys is not transformed into filaments completely and the detailed value is still unknown. Thus, this formula is not applicable to the strength calculation of low strain processing.

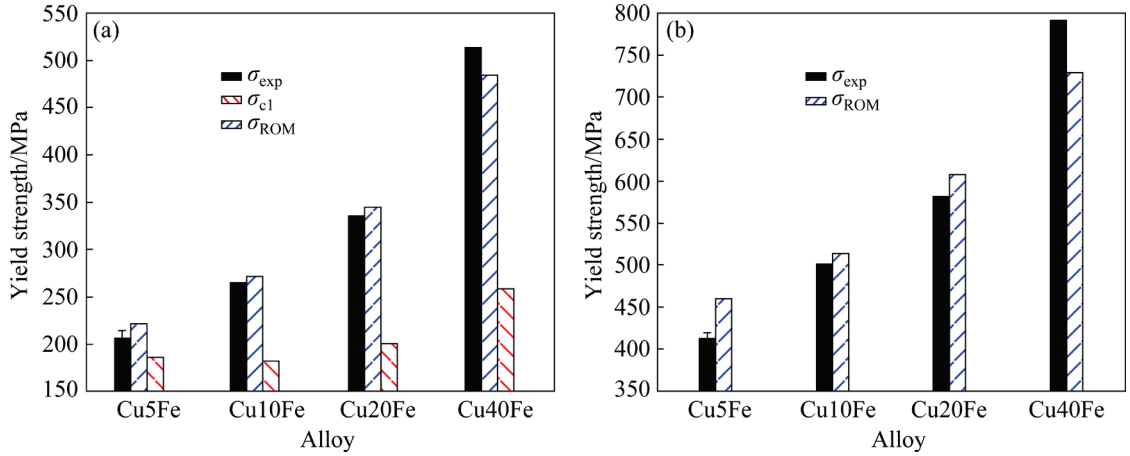

Fig. 15 Experimental values of yield strength (σ_{exp}), calculated values of yield strength (σ_{c1}) by Cu alloys formulas, and calculated values (σ_{ROM}) by ROM of different alloys: (a) SPS-ed Cu−Fe alloys; (b) Cu−Fe alloys after CR+AG

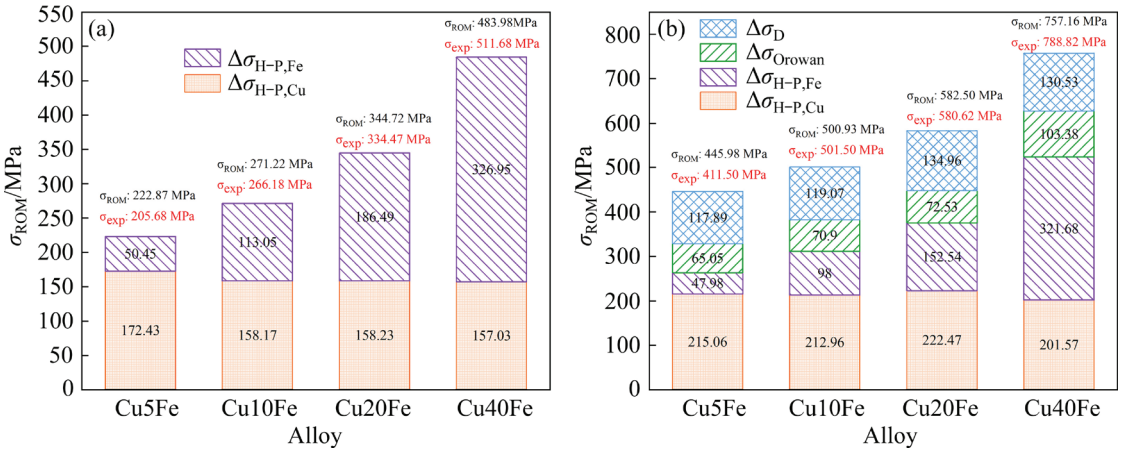

Fig. 16 Calculated values (σ_{ROM}) by ROM of SPS-ed Cu−Fe alloys (a) and Cu−Fe alloys after CR+AG (b)

In the previous discussion, it can be found that the ROM can match well with the strength calculation of Cu−Fe alloys before deformation. Therefore, ROM is used to calculate the yield strength of Cu−Fe alloy under low strain deformation in this work. The structures of the alloys are composed of Cu matrix, primary Fe phase and secondary Fe phase. Hence, individual contributions of these three parts to the total strength were calculated respectively, and then three parts were summed up to get the total calculated strength.

Cu20Fe alloy after cold-rolling and aging was selected as an example to calculate the yield strength by using ROM. The main strengthening mechanisms of Cu matrix are the grain boundary strengthening ($\Delta\sigma_{H-P,Cu}$) and the dislocation strengthening ($\Delta\sigma_D$). Fe phases can be divided into primary Fe phase and secondary Fe phase. The size of the primary Fe phase is in the micron level, and fine Fe phase is formed at the grain boundary of Cu. With the increase of Fe content, the number and size of Fe grains increase (Figs. 12 and 13). The strengthening mechanism of primary Fe phase is grain boundary strengthening ($\Delta\sigma_{H-P,Fe}$). The strengthening mechanism of secondary Fe particles, namely the precipitated Fe phase, is Orowan strengthening mechanism ($\Delta\sigma_{Orowan}$).

(1) Grain boundary strengthening of Cu matrix and primary Fe phase

In the SPS-ed state, the yield strength of grain boundary strengthening calculated by ROM is basically consistent with the experimental value (shown in Fig. 15(a)). Therefore, the above formulas (Eqs. (3) and (4)) are still used in the calculation of grain boundary strengthening of Cu phase and primary Fe phase in the deformed state, respectively.

(2) Dislocation strengthening of Cu matrix

The dislocation density was obtained by XRD. The strengthening value of the dislocation is calculated by

$$\Delta\sigma_D = M\alpha Gb\rho^{1/2} \tag{7}$$

where M is Taylor factor, G is the shear modulus of Cu matrix, α is a constant, b is the amplitude of Burgers vector, and ρ is the dislocation density, which can be calculated by the Williamson−Hall method $\rho=16.1\varepsilon^2/b^2$ [38], where ε is micro-strain obtained from XRD results of the sample.

(3) Precipitation strengthening of Fe precipitates

Precipitation strengthening can be calculated by [8,38]

$$\Delta\sigma_{Orowan} = 0.81\frac{MGb}{2\pi(1-\nu)^{1/2}}\cdot\frac{\ln(d_p/b)}{\frac{1}{2}d_p\sqrt{\frac{3\pi}{2f_v}-d_p}} \tag{8}$$

where ν is the Poisson's ratio, f_v is the volume fraction of Fe precipitates, and d_p is the average size of the dispersed Fe precipitates measured under TEM.

The total yield strength of the alloys after cold-rolling and aging can be calculated by

$$\sigma_{ROM}=\Delta\sigma_{H-P,Cu}+\Delta\sigma_{H-P,Fe}+\Delta\sigma_{Orowan}+\Delta\sigma_D \tag{9}$$

The detailed values of the parameters during the above calculation are tabulated in Table 2.

As shown in Fig. 15(b), the calculated values of the alloys are in good agreement with the experimental values. The contributions of strength from each strengthening mechanism as calculated

from Eqs. (3) and (4) and Eqs. (7)−(9) are given in Fig. 16(b) for the Cu−Fe alloys after cold rolling and subsequent aging at 450 °C for 6 h. Compared with Fig. 16(a), after rolling and aging treatments, the strengthening mechanisms of the Cu−Fe alloy are grain boundary strengthening, Orowan strengthening and dislocation strengthening. The contribution of grain boundary strengthening of Cu matrix and Fe phase to yield strength can reach 60%−70%, which is the main strengthening factor. With increasing Fe content, the increase of strength mainly comes from the grain boundary strengthening ($\Delta\sigma_{H-P,Fe}$) and the precipitation strengthening ($\Delta\sigma_{Orowan}$). With increasing Fe content, the primary Fe phase and secondary Fe phase have increasing volume fractions, and the strengthening effect is enhanced. In these two strengthening methods, the grain boundary strengthening caused by primary Fe phase is the dominant factor, because most of the Fe in the alloy exists in the form of primary Fe phase. This suggests the key role of the primary Fe phase in improving the yield strength of Cu−Fe alloys, as schematically illustrated in Fig. 17. To be specific, in Cu5Fe and Cu10Fe alloys, the Fe phase particles exist in Cu GBs or Cu grains to impede the dislocation movement, thus improving the strength of the alloy. When the Fe content is higher than 20 wt.%, the primary Fe phase exists in the form of coarse particles, and some Fe grains appear. These Fe grains can store a large number of dislocations, and also contain some copper phases to hinder the movement of dislocations. Fe grains with high strength exist in the alloy, effectively improving the strength of the alloy. A lot of Fe grains and Fe particles are in Cu40Fe alloy, and the double-strengthening effect greatly improves the strength of the alloy.

Table 2 Parameters used in yield strength model of Cu20Fe after cold rolling and aging at 450 °C for 6 h

Parameter	Value	Source
k_{Cu}/(MPa·m$^{1/2}$)	0.18	[31]
$d_{grain,Cu}$/μm	0.61	This work
φ_{Cu}/%	79.32	This work
$\Delta\sigma_{H-P,Cu}$/MPa	222.47	This work
k_{Fe}/(MPa·m$^{1/2}$)	0.6	[33]
$d_{grain,Fe}$/μm	0.75	This work
φ(primary Fe phase)/%	19.24	This work
$\Delta\sigma_{H-P,Fe}$/MPa	152.54	This work
M	3.1	[38]
G/GPa	46	[38]
b/nm	0.2556	[38]
v	0.34	[38]
d_p/nm	52.14	This work
f_v/%	1.44	This work
$\Delta\sigma_{Orowan}$/MPa	72.53	This work
ρ/m^{-2}	3.4×10^{14}	This work
$\Delta\sigma_D$/MPa	134.96	This work
$\Delta\sigma_{ROM}$/MPa	582.50	This work

4.3 Effect of Fe content on electrical properties of Cu−Fe alloys

In addition to segregation, low conductivity also restricts the application of Cu−Fe alloys. Among many alloying elements of Cu alloys, Fe

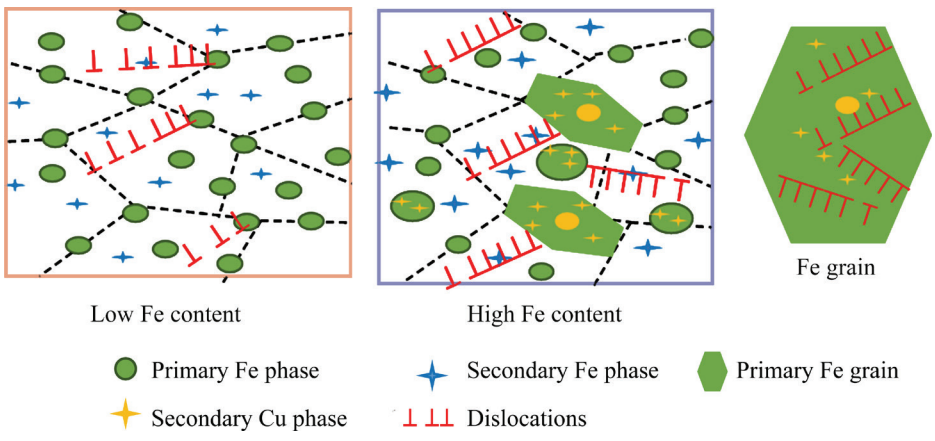

Fig. 17 Schematic diagrams showing dislocation pile-up mechanism of Cu−Fe alloys with low and high Fe contents

greatly damages the conductivity of Cu alloys. The electrical resistivity increases by 9.2 μΩ/cm for every 1 wt.% Fe solution in the Cu matrix. The resistance for Cu-based alloys comes from the scattering of electrons in motion. The scattering mainly comes from phonon scattering, dislocation scattering, interface scattering (the Cu−Fe interface and grain boundaries) and impurity atoms (Fe atoms) scattering as follows [39]:

$$\rho_{total}=\rho_{phonon}+\rho_{dislocations}+\rho_{interface}+\rho_{impurities} \quad (10)$$

The scattering from impurity atoms ($\rho_{impurities}$) plays a dominant role, so it is important to reduce the residual Fe atoms in Cu matrix as much as possible to improve the conductivity [40]. In this work, after aging at 450 °C for 16 h, the conductivity of the cold rolled sample increases and tends to be stable. After cold deformation and aging treatment, electrical conductivity (EC) of the four alloys is increased by more than 50%. During the aging process, Fe solution atoms in Cu matrix can be transferred to the precipitation or nucleation part of the precipitation through the dislocation network, which can increase the EC [41]. The relationship among diffusion coefficients of Fe solution atoms during aging is as follows:

$$D_0=D_L(1-\varphi)+D_p\varphi \quad (11)$$

where D_0 is the diffusion coefficient, D_L is the diffusion coefficient of the lattice, φ is the volume fraction of atoms in the dislocation, and D_p is the diffusion coefficient of atoms in the dislocation. The diffusion coefficient of atoms in dislocation D_p is much larger than that in lattice D_L. The dislocation density is increased after cold deformation and dislocation networks provide fast channels for the diffusion of Fe atoms during the precipitation process. Therefore, after aging, the scattering from impurity atoms ($\rho_{impurities}$) reduces, and the conductivity increases.

5 Conclusions

(1) With the increase of Fe content, the size of primary Fe phase increases (from 0.29 to 1.2 μm), and the primary Fe phase is evenly distributed without aggregating into coarse Fe phase.

(2) After cold rolling and aging treatments, the yield strength and electrical conductivity of Cu−Fe alloys are increased by more than 50%.

(3) For the SPS-ed Cu−Fe alloys, the grain boundary strengthening is the main strengthening mechanism. The rule of mixture accurately predicts the actual yield strength of Cu−Fe alloys.

(4) For the Cu−Fe alloys after cold rolling and aging treatments, a novel method is used to calculate the respective contributions of Cu matrix, primary Fe phase and secondary Fe phase to the yield strength. The calculated results agree well with the experimental results.

CRediT authorship contribution statement

Ping ZHANG: Experiment, Writing − Original draft; **Xiao-bo YUAN:** Methodology, Investigation; **Zi-ming ZENG:** Investigation; **Jian-wei TENG:** Supervision; **Yun-he ZHOU:** Supervision; **Biao-biao YANG:** Writing − Review & editing; **Yun-ping LI:** Supervision, Writing − Review & editing.

Declaration of competing interest

The authors declare that they have no known competing financial interests or personal relationships that could have appeared to influence the work reported in this paper.

Acknowledgments

The authors are grateful for the financial supports from the Natural Science Foundation of China (No. 51871244), the Hunan Provincial Innovation Foundation for Postgraduate, China (No. CX20200172), and the Fundamental Research Funds for the Central Universities of Central South University, China (No. 1053320190103).

References

[1] ZHANG Chen-zeng, CHEN Cun-guang, LIU Xin-hua, YAN Meng-jie, QI Miao, LI Xue-cheng, LI Yang, ZHANG Hai-feng, YANG Fang, WANG Wen-wen, GUO Zhi-meng. High strength and high electrical conductivity in Cu−Fe alloys with nano and micro Fe particles [J]. Materials Science and Engineering: A, 2022, 855: 143948.

[2] WANG Meng, YANG Qian-ru, JIANG Yan-bin, LI Zhou, XIAO Zhu, GONG Shen, WANG Yong-ru, GUO Chuang-li, WEI Hai-gen. Effects of Fe content on microstructure and properties of Cu−Fe alloy [J]. Transactions of Nonferrous Metals Society of China, 2021, 31(10): 3039−3049.

[3] YUAN Da-wei, ZENG Hao, XIAO Xiang-peng, WANG Hang, HAN Bao-jun, LIU Bai-xiong, YANG Bin. Effect of Mg addition on Fe phase morphology, distribution and aging kinetics of Cu−6.5Fe alloy [J]. Materials Science and Engineering: A, 2021, 812: 141064.

[4] ZHANG Ping, YUAN Xiao-bo, LI Yi-di, ZHOU Yun-he, LAI Rui-lin, LI Yun-ping, LEI Qian, CHIBA A. Influence of minor Ag addition on the microstructure and properties of

powder metallurgy Cu−10wt.%Fe alloy [J]. Journal of Alloys and Compounds, 2022, 904: 163983.

[5] LU De-ping, WANG Jun, ZENG Wei-jun, LIU Yong, LU Lei, SUN Bao-de. Study on high-strength and high-conductivity Cu−Fe−P alloys [J]. Materials Science and Engineering: A, 2006, 421(1/2): 254−259.

[6] ZHENG Yan-xin, LIU Ying, ZHENG Feng, SONG Qing-song, ZHANG Cai-li, WANG Jian, DONG Nan, SHI Ai-juan, HAN Pei-de. Effects of iron content on tribological properties of Cu−Fe-based friction material [J]. Industrial Lubrication and Tribology, 2019, 71(5): 718−723.

[7] JEONG Y B, JO H R, KIM J T, HONG S H, KIM K B. A study on the micro-evolution of mechanical property and microstructures in (Cu−30Fe)−2X alloys with the addition of minor alloying elements [J]. Journal of Alloys and Compounds, 2019, 786: 341−345.

[8] WANG Meng, ZHANG Rui, XIAO Zhu, GONG Shen, JIANG Yan-bin, LI Zhou. Microstructure and properties of Cu−10wt.%Fe alloy produced by double melt mixed casting and multi-stage thermomechanical treatment [J]. Journal of Alloys and Compounds, 2020, 820: 153323.

[9] PANG Yong-jie, CHAO Guo-hui, LUAN Tian-yang, GONG Shen, WANG Yong-ru, JIANG Zhao-han, XIAO Zhu, JIANG Yan-bin, LI Zhou. Microstructure and properties of high strength, high conductivity and magnetic Cu−10Fe−0.4Si alloy [J]. Materials Science and Engineering: A, 2021, 826: 142012.

[10] LIU Shi-chao, XU Song-song, JIE Jin-chuan, ZHANG Jun-jia, DONG Yong, LI Xin-zhong, LI Ting-ju. Microstructure evolution and magnetic properties of metastable immiscible Cu−Fe alloy with micro-alloying B element [J]. Journal of Alloys and Compounds, 2021, 888: 161627.

[11] ZHANG Chen-zeng, CHEN Cun-guang, LI Pei, YAN Meng-jie, QIN Qian, YANG Fang, WANG Wen-wen, GUO Zhi-meng, VOLINSKY A A. Microstructure and properties evolution of rolled powder metallurgy Cu−30Fe alloy [J]. Journal of Alloys and Compounds, 2022, 909: 164761.

[12] LUO S B, WANG W L, CHANG J, XIA Z C, WEI B. A comparative study of dendritic growth within undercooled liquid pure Fe and Fe50Cu50 alloy [J]. Acta Materialia, 2014, 69: 355−364.

[13] MULLIS A M, JEGEDE O E, BIGG T D, COCHRANE R F. Dynamics of core–shell particle formation in drop-tube processed metastable monotectic alloys [J]. Acta Materialia, 2020, 188: 591−598.

[14] WANG F L, WAKOH K, LI Y P, ITO S, YAMANAKA K, KOIZUMI Y, CHIBA A. Study of microstructure evolution and properties of Cu−Fe microcomposites produced by a pre-alloyed powder method [J]. Materials & Design, 2017, 126: 64−72.

[15] LI Yi-di, YUAN Xiao-bo, YANG Biao-biao, YE Xian-jue, ZHANG Ping, LANG Hao-yu, LEI Qian, LIU Jian-tao, LI Yun-ping. Hierarchical microstructure and strengthening mechanism of Cu−36.8Fe alloy manufactured by selective laser melting [J]. Journal of Alloys and Compounds, 2022, 895: 162701.

[16] SHUKLA A K, SAMUEL M G, SURESH KUMAR R, NARAYANA MURTY S V S, MONDAL K. Effect of powder oxidation on densification and properties of vacuum hot pressed Cu−Cr−Nb alloy [J]. Materials Science and Engineering: A, 2013, 561: 452−459.

[17] NIU Tong-jun, ZHANG Yi-fan, CHO J, LI Jin, WANG Hai-yan, ZHANG Xing-hang. Thermal stability of immiscible Cu−Ag/Fe triphase multilayers with triple junctions [J]. Acta Materialia, 2021, 208: 116679.

[18] BAMBERGER M, MUNITZ A, KAUFMAN L, ABBASCHIAN R. Evaluation of the stable and metastable Cu−Co−Fe phase diagrams [J]. Calphad, 2002, 26(3): 375−384.

[19] PEREZ M, DUMONT M, ACEVEDO-REYES D. Implementation of classical nucleation and growth theories for precipitation [J]. Acta Materialia, 2008, 56(9): 2119−2132.

[20] LACH T G, FRAZIER W E, WANG J, DEVARAJ A, BYUN T S. Precipitation-site competition in duplex stainless steels: Cu clusters vs spinodal decomposition interfaces as nucleation sites during thermal aging [J]. Acta Materialia, 2020, 196: 456−469.

[21] LU Lei, SHEN Yong-feng, CHEN Xian-hua, QIAN Li-hua, LU K. Ultrahigh strength and high electrical conductivity in copper [J]. Science, 2004, 304(5669): 422−426.

[22] ZHANG Ping, LEI Qian, YUAN Xiao-bo, SHENG Xiao-fei, JIANG Dong, LI Yun-ping, LI Zhou. Microstructure and mechanical properties of a Cu−Fe−Nb alloy with a high product of the strength times the elongation [J]. Materials Today Communications, 2020, 25: 101353.

[23] SHI R P, WANG C P, WHEELER D, LIU X J, WANG Y. Formation mechanisms of self-organized core/shell and core/shell/corona microstructures in liquid droplets of immiscible alloys [J]. Acta Materialia, 2013, 61(4): 1229−1243.

[24] CUI S L, JUNG I H. Thermodynamic modeling of the Cu−Fe−Cr and Cu−Fe−Mn systems [J]. Calphad, 2017, 56: 241−259.

[25] TIAN Y Z, REN Y P, GAO S, ZHENG R X, WANG J H, PAN H C, ZHANG Z F, TSUJI N, QIN G W. Two-stage Hall−Petch relationship in Cu with recrystallized structure [J]. Journal of Materials Science & Technology, 2020, 48: 31−35.

[26] BISELLI C, MORRIS D G. Microstructure and strength of Cu−Fe in situ composites after very high drawing strains [J]. Acta Materialia, 1996, 44(2): 493−504.

[27] STEPANOV N D, KUZNETSOV A V, SALISHCHEV G A, KHLEBOVA N E, PANTSYRNY V I. Evolution of microstructure and mechanical properties in Cu−14%Fe alloy during severe cold rolling [J]. Materials Science and Engineering: A, 2013, 564: 264−272.

[28] YANG Fei, DONG Li-ming, ZHOU Li-chu, ZHANG Ning, ZHOU Xue-feng, ZHANG Xiao-dan, FANG Feng. Excellent strength and electrical conductivity achieved by optimizing the dual-phase structure in Cu−Fe wires [J]. Materials Science and Engineering: A, 2022, 849: 143484.

[29] LI Yi-di, YANG Biao-biao, ZHANG Ping, NIE Yan, YUAN Xiao-bo, LEI Qian, LI Yun-ping. Cu−Cr−Mg alloy with both high strength and high electrical conductivity manufactured by powder metallurgy process [J]. Materials Today Communications, 2021, 27: 102266.

[30] ZHANG Shuang, WANG Fei, HUANG Ping. Enhanced

Hall−Petch strengthening in graphene/Cu nanocomposites [J]. Journal of Materials Science & Technology, 2021, 87: 176−183.
[31] HANSEN N. Hall−Petch relation and boundary strengthening [J]. Scripta Materialia, 2004, 51(8): 801−806.
[32] RABADIA C D, LIU Y J, JAWED S F, WANG L, LI Y H, ZHANG X H, SERCOMBE T B, SUN H, ZHANG L C. Improved deformation behavior in Ti−Zr−Fe−Mn alloys comprising the C14 type Laves and β phases [J]. Materials & Design, 2018, 160: 1059−1070.
[33] TAKEDA K, NAKADA N, TSUCHIYAMA T, TAKAKI S. Effect of interstitial elements on Hall−Petch coefficient of ferritic iron [J]. ISIJ International, 2008, 48(8): 1122−1125.
[34] CALCAGNOTTO M, PONGE D, RAABE D. Effect of grain refinement to 1μm on strength and toughness of dual-phase steels [J]. Materials Science and Engineering: A, 2010, 527(29/30): 7832−7840.
[35] IRANI H, SHABAN GHAZANI M. Effect of grain refinement on tensile properties and electrochemical behavior of Fe−18.5%Cr ferritic stainless steel [J]. Materials Chemistry and Physics, 2020, 251: 123089.
[36] SONG J S, HONG S I, KIM H S. Heavily drawn Cu–Fe−Ag and Cu−Fe−Cr microcomposites [J]. Journal of Materials Processing Technology, 2001, 113(1/2/3): 610−616.
[37] RAABE D, OHSAKI S, HONO K. Mechanical alloying and amorphization in Cu−Nb−Ag in situ composite wires studied by transmission electron microscopy and atom probe tomography [J]. Acta Materialia, 2009, 57(17): 5254−5263.
[38] HUANG Jia-zhen, XIAO Zhu, DAI Jie, LI Zhou, JIANG Hong-yun, WANG Wei, ZHANG Xiao-xuan. Microstructure and properties of a novel Cu−Ni−Co−Si−Mg alloy with super-high strength and conductivity [J]. Materials Science and Engineering: A, 2019, 744: 754−763.
[39] VERHOEVEN J D, DOWNING H L, CHUMBLEY L S, GIBSON E D. The resistivity and microstructure of heavily drawn Cu−Nb alloys [J]. Journal of Applied Physics, 1989, 65(3): 1293−1301.
[40] XIE Zhi-xiong, GAO Hai-yan, DONG S J, WANG J, HUANG H, LUO Ping. Enhanced strength and electrical conductivity of Cu−8Fe composite by adding trace Ag and P [J]. Materials Transactions, 2013, 54(11): 2075−2078.
[41] HUMPHREYS F J, HIRSCH P B. The deformation of single crystals of copper and copper-zinc alloys containing alumina particles — II: Microstructure and dislocation−particle interactions [J]. Mathematical and Physical Sciences, 1970, 318(1532): 73−92.

Fe 含量对粉末冶金 Cu−Fe 合金显微组织与性能的影响

张 平[1]，袁晓波[1]，曾梓名[1]，滕剑威[1]，周芸合[2]，杨标标[1,3,4]，李云平[1]

1. 中南大学 粉末冶金国家重点实验室，长沙 410083；
2. Institute for Materials Research, Tohoku University, Sendai 980-8577, Japan;
3. IMDEA Materials Institute, C/Eric Kandel 2, Getafe, Madrid 28906, Spain;
4. Department of Materials Science, Polytechnic University of Madrid/Universidad Politécnica de Madrid, E.T.S. de Ingenieros de Caminos, Madrid 28040, Spain

摘 要：研究 Fe 含量对粉末冶金 Cu−Fe 合金显微组织及性能的影响。采用电火花等离子烧结、冷轧以及时效处理工艺制备 4 种不同铁含量 (5%、10%、20%和 40%，质量分数)的 Cu−Fe 合金。研究结果表明，随着 Fe 含量从 5% (质量分数)增加到 40% (质量分数)，Fe 相由离散球形分布演变为连续交错分布，Fe 相尺寸从 0.29 μm 增加到 1.20 μm；时效态的 Cu−Fe 合金的屈服强度从 411.5 MPa 提高到 788.8 MPa，电导率从 62.5% (IACS)降低到 42.0% (IACS)。在以上结果的基础上，提出一种混合法则计算 Cu 基体、初级 Fe 相和次级 Fe 相对屈服强度的贡献，可较好地预测 Fe 含量高于 10% (质量分数)合金的力学性能。

关键词：铜铁合金；粉末冶金；快速凝固；力学性能；强度计算

(Edited by Wei-ping CHEN)